J. Phys. Chem. B **2005,** *109,* 8861−8872

Air−Liquid Interfaces of Aqueous Solutions Containing Ammonium and Sulfate: Spectroscopic and Molecular Dynamics Studies

Sandhya Gopalakrishnan,[†] **Pavel Jungwirth,**[‡] **Douglas J. Tobias,**[§] **and Heather C. Allen***[,†]

Department of Chemistry, The Ohio State University, 100 W. 18th Avenue, Columbus, Ohio 43210, Institute of Organic Chemistry and Biochemistry, Academy of Sciences of the Czech Republic and Center for Biomolecules and Complex Molecular Systems, Flemingovo nam. 2, 16610 Prague 6, Czech Republic, and Department of Chemistry, University of California, Irvine, Irvine, California 92697-2025.

Received: January 3, 2005; In Final Form: February 25, 2005

Investigations of the air−liquid interface of aqueous salt solutions containing ammonium (NH_4^+) and sulfate (SO_4^{2-}) ions were carried out using molecular dynamics simulations and vibrational sum frequency generation spectroscopy. The molecular dynamics simulations show that the predominant effect of SO_4^{2-} ions, which are strongly repelled from the surface, is to increase the thickness of the interfacial region. The vibrational spectra reported are in the O−H stretching region of liquid water. Isotropic Raman and ATR-FTIR (attenuated total reflection Fourier transform infrared) spectroscopies were used to study the effect of ammonium and sulfate ions on the bulk structure of water, whereas surface sum frequency generation spectroscopy was used to study the effect of these ions on the interfacial structure of water. Analysis of the interfacial and bulk vibrational spectra reveal that aqueous solutions containing SO_4^{2-} perturb the interfacial water structure differently than the bulk and, consistent with the molecular dynamics simulations, reveal an increase in the thickness of the interfacial region.

Introduction

It is well-known that aerosols can affect the earth's climate directly by scattering and absorbing radiation and indirectly by serving as cloud condensation nuclei (CCN), thereby modifying the optical properties and lifetimes of clouds.[1−3] To develop accurate models to predict climate change, it is important to consider the optical properties, which are influenced by composition and growth of aerosols. The concentration of sulfuric acid in tropospheric aerosols is typically greater than 40 wt % and can be neutralized by gaseous ammonia to form NH_4HSO_4 and $(NH_4)_2SO_4$.[4] Several studies have shown that ammonium sulfate aerosols are abundant in the atmosphere;[5−8] Talbot et al. have measured comparable amounts of NH_4^+ and SO_4^{2-} in tropospheric aerosols.[9]

Sulfate aerosols are important in the context of aerosol transformation and growth. For example, ammonium sulfate aerosols play an important part in the heterogeneous hydrolysis of N_2O_5 to form nitric acid. A recent report by Kane et al.[10] shows that the uptake of N_2O_5 by $(NH_4)_2SO_4$ and NH_4HSO_4 aerosols is significant at relative humidity of >50%, showing that the process is governed by the presence of water in these aerosols. Kane et al. further postulate that the reaction primarily takes place with the water at the surface of the aerosol. However, the mechanism for this reaction is still unknown. Several recent studies have proposed that it is the interface that governs much of the chemistry in aerosols.[11−13] The above example hints that the hydrolysis of N_2O_5 can be catalyzed by the presence of interfacial water (as opposed to ammonium or sulfate). Knowledge of the molecular structure of the interface of aerosols can help to elucidate the reaction mechanism at the interface. The work described in this paper addresses fundamental issues regarding the interfacial molecular structure of aerosols containing ammonium and sulfate.

Surface tension measurements provide macroscopic information about the concentration changes (with respect to the bulk) in the surface region of aqueous salt solutions. Namely, the increase of surface tension of simple inorganic salt solutions compared to neat water is related via the Gibbs adsorption equation to a net decrease of ionic concentration in the interface. However, surface tension data provide only an integrated value of the ionic deficit over the whole interfacial region, which can be several molecular layers thick. To obtain more refined and detailed information about the distribution of ions at the air/water interface, in addition to conducting surface tension measurements, we have combined the surface-selective technique of vibrational sum frequency generation (SFG) spectroscopy with molecular dynamics (MD) simulations of extended aqueous slabs containing molar concentrations of ammonium sulfate, sodium sulfate, and ammonium chloride.

Sum Frequency Generation Background

The theory of SFG has been described extensively in the literature.[14−18] Only a brief overview will be presented here. SFG is a second-order nonlinear process that occurs in non-centrosymmetric environments such as interfaces under the electric-dipole approximation. The SFG intensity, I_{SFG}, is shown in eq 1a

$$I^{\omega_{SFG}}(\omega) \propto |E^{\omega_{SFG}}\cdot\chi^{(2)}:E^{\omega_{vis}}E^{\omega_{IR}}|^2 I^{\omega_{vis}}I^{\omega_{IR}} \qquad (1a)$$

where $I^{\omega_{SFG}}(\omega)$ is the intensity of the SFG and is a function of the frequency ω, $I^{\omega_{vis}}I^{\omega_{IR}}$ is the intensity of the incident visible

---

[*] To whom correspondence should be addressed: allen@chemistry.ohio-state.edu.

[†] The Ohio State University.

[‡] Academy of Sciences of the Czech Republic and Center for Biomolecules and Complex Molecular Systems; pavel.jungwirth@uochb.cas.cz.

[§] University of California, Irvine.

10.1021/jp0500236 CCC: $30.25

multiplied by the incident IR, and $|E^{\omega_{\mathrm{SFG}}}.\chi^{(2)}:E^{\omega_{\mathrm{vis}}}E^{\omega_{\mathrm{IR}}}|^2$ is the absolute square of the E field at the interface denoted by superscripts that define the frequency of the exigent (SFG) and incident (visible and IR) frequencies. *E* includes the Fresnel terms. $\chi^{(2)}$ is the tensor that describes the macroscopic susceptibility of the system. $\chi^{(2)}$ is expanded in eq 1b to

$$|\chi^{(2)}|^2 = |\chi^{(2)}_{\mathrm{NR}} + \sum_{\nu}\chi^{(2)}_{\nu}|^2 \tag{1b}$$

The macroscopic second-order susceptibility, $\chi^{(2)}$, consists of a nonresonant term ($\chi_{\mathrm{NR}}{}^{(2)}$) and resonant terms ($\chi^{(2)}_{\nu}$). When the frequency of an incident infrared beam,ω_{IR}, is resonant with a vibrational mode of an interfacial molecule, ν, the resonant susceptibility term $\chi^{(2)}_{\nu}$ dominates $\chi^{(2)}$, and an SFG intensity enhancement is observed. $\chi^{(2)}_{\nu}$ is given below in eq 2

$$\chi^{(2)}_{\nu} \propto \frac{A_{\nu}}{\omega_{\nu} - \omega_{\mathrm{IR}} - i\Gamma_{\nu}} \tag{2}$$

where A_ν is the amplitude of the SFG transition moment, ω_ν is the frequency of the transition, and Γ_ν describes the line-width of the transition. The amplitude, A_ν, is nonzero when the Raman and IR transitions are spectroscopically allowed. The macroscopic nonlinear susceptibility $\chi^{(2)}$ is related to the molecular susceptibility, $\beta_{lmn,\nu}$. The molecular susceptibility can be described by eq 3

$$\beta_{lmn,\nu} = \frac{\langle g|\alpha_{lm}|\nu\rangle\langle\nu|\mu_n|g\rangle}{\omega_{\mathrm{IR}} - \omega_{\nu} + i\Gamma_{\nu}} \tag{3}$$

where $\langle g|\alpha_{lm}|\nu\rangle$ represents the Raman tensor for the transition, $\langle\nu|\mu_n|g\rangle$ represents the IR transition moment for the molecule, and *lmn* represents the molecule fixed axes. An Euler angle transformation relates the laboratory coordinate system (*I, J, K*) to the molecular coordinate system (*l, m, n*). The transformation is shown in eq 4

$$\beta_{IJK,\nu} = \sum_{lmn}\mu_{IJK:lmn}\beta_{lmn,\nu} \tag{4}$$

where $\mu_{IJK:lmn}$ is the Euler angle transformation between the laboratory coordinates (*I, J, K*) and the molecular coordinates (*l, m, n*). The macroscopic susceptibility, $\chi^{(2)}_{IJK,\nu}$, is therefore calculated from the molecular susceptibility, $\beta_{IJK,\nu}$, as shown in eq 5

$$\chi^{(2)}_{IJK,\nu} = N\langle\beta_{IJK,\nu}\rangle \tag{5}$$

where $\chi_{IJK,\nu}$ is equal to the number density, *N*, multiplied by the ensemble average of $\beta_{IJK,\nu}$.

Recasting eq 5

$$\chi^{(2)}_{IJK,\nu} = N\sum_{lmn}\langle\mu_{IJK:lmn}\rangle\beta_{lmn,\nu} = N\sum_{lmn}\langle\mu_{IJK:lmn}\rangle\frac{\langle g|\alpha_{lm}|\nu\rangle\langle\nu|\mu_n|g\rangle}{\omega_{\mathrm{IR}} - \omega_{\nu} + i\Gamma_{\nu}} \tag{6}$$

For a single vibrational mode, we can ignore phase; thus, from eqs 1 and 6, we have

$$I^{\nu}_{\mathrm{SFG}} \propto N^2(\sum_{lmn}\langle\mu_{IJK:lmn}\rangle|\langle g|\alpha_{lm}|\nu\rangle\langle\nu|\mu_n|g\rangle|)^2 \tag{7}$$

Equation 7 relates the SFG intensity to the Raman tensor and IR transition moment for the transition (the square of each integral is the intensity) for a single vibrational mode.

Experimental Section

SFG Spectra. The air−liquid interface in the O−H stretching region of water (2800−3900 cm^{-1}) was probed using a scanning SFG system which has been described in detail elsewhere.[19] Essentially, the scanning SFG system uses a 532 nm frequency-doubled output of an Nd:YAG laser (EKSPLA PL 2143 A/SS, 10 Hz repetition rate, 29 ps pulse duration) and an IR beam from a KTP/KTA-based optical parametric generator/amplifier (OPG/OPA, Laservision). The IR beam is tunable from 2500 to 4000 cm^{-1} and has a bandwidth of ∼8 cm^{-1}. The 532 nm beam is focused on the liquid surface using a plano-convex lens to yield a beam diameter of ∼1 mm with a pulse energy of ∼400 μJ. The IR beam is focused near the sample surface using a BaF_2 lens to yield a diameter of <0.5 mm. The peak IR energy (at ∼3400 cm^{-1}) was ∼400 μJ. The IR profile was measured simultaneously with the SFG spectrum by reflecting ∼5% of the beam intensity onto an IR energy meter (Molectron-Coherent J9LP) using a BaF_2 window.

The input angles were ∼48° and ∼57° for the 532 nm and IR beams, respectively, from the surface normal. The detection angle was set to ∼51° from the surface normal for sum frequency. A 512 × 512 pixel thermoelectrically cooled back-illuminated charge-coupled device (CCD) (DV412, Andor Technology) was used to detect the sum frequency signal. A series of apertures were used to block the 532 nm (and IR) beam and only allow the sum frequency beam to be detected. In addition, a series of notch and short-pass optics were used to filter out the scattered 532 nm light.

The SFG spectra presented here were acquired using a 15 s exposure time per data point, leading to an acquisition time of ∼30 min for the spectral range of 2800−3900 cm^{-1}. An average of four replicate spectra are presented in each case. Spectra of neat water were acquired at least once before and after each salt solution to confirm reproducibility. The polarization combination used for the SFG spectra was S, S, and P for sum frequency, visible, and IR, respectively, where S polarization has its E field vector perpendicular to the incident plane and P polarization has its E field vector parallel to the incident plane. The SFG spectra were calibrated using the IR absorption spectrum of a polystyrene film, and the error in determining the absolute IR frequency was ±3 cm^{-1}.

It is desirable that the SFG spectra be normalized to take into account temporal and spatial overlap anomalies over the entire spectral region. Normalizing the SFG spectra to the sum frequency response from a GaAs crystal can do this. However, the IR profile can change slightly from one spectrum to another, and because we currently do not monitor the SFG from the GaAs crystal as well as the air−liquid interface simultaneously, the spectra shown in this paper were normalized to the IR profile. Spectra were also normalized to the GaAs crystal and found to be comparable to those normalized to the IR profile.

Raman Spectra. Raman spectra were obtained using unpolarized light and polarized light in separate studies conducted at ∼24 °C. Unpolarized Raman spectra were acquired using a 532 nm continuous wave (CW) YAG laser (Spectra Physics, Millenia II), a 5 mm focusing Raman probe (InPhotonics, RP 532-05-15-FC), a 500 mm monochromator (Acton Research, SpectraPro SP-500) using a 1200 groove/mm grating, and a back-illuminated CCD (Roper Scientific, LN400EB, 1340 × 400 pixel array and deep depletion). The collection fiber optic (which is part of the InPhotonics Raman probe) was coupled to the entrance slit of the monochromator. The power of the 532 nm beam was ∼250 mW. The monochromator was calibrated using the 435.83 nm line from fluorescent light and was verified by comparison to the Raman spectrum of naphthalene.

Polarized Raman studies (isotropic and anisotropic) were completed by passing collimated (∼1 mm diameter beam) vertically polarized light from the YAG laser (∼200 mW) onto the sample and detecting the scatter with the Raman probe. A 90° configuration for the incoming laser beam and detection was used. A sheet polarizer was placed between the sample and the probe to select the polarization of the Raman scatter. The band-pass for all Raman experiments was ~ 3 cm^{-1}.

ATR-FTIR Spectra. ATR-FTIR spectra were obtained using a Thermo Nicolet spectrometer (Avatar 370, Thermo Electron Corporation). A 45° single-bounce ZnSe crystal trough mounted on an accessory (Smart SpeculATR) was used to collect spectra at a resolution of 4 cm^{-1} and averaged over 32 scans at ∼24 °C.

Spectral Fits. The SFG spectrum, which is a plot of the SFG intensity (I_{SFG}) as a function of the incident infrared frequency (ν), can be mathematically fit according to eq 2. When performing the fit, a constant complex number is used as the nonresonant term ($\chi^{(2)}_{NR}$) and the sign of the amplitude (A_ν) is used to denote the phase of the photons of the vibrational mode from the interfacial molecules, which incorporates orientation and relative vibrational phases. Equation 2 indicates the Lorentzian line shape in the SFG spectrum fitting. In Raman and IR spectroscopy, the intensity is the summation of the intensity of each vibration, while in SFG the intensity is proportional to the absolute square of the summation of the $\chi^{(2)}_\nu$ and $\chi^{(2)}_{NR}$ of each vibration as shown in eq 1b. This leads to different spectral character for SFG spectra relative to Raman and IR spectra. Therefore, SFG spectral interpretation must occur after deconvolution into the component peaks, because direct comparison of SFG spectra to Raman and IR spectra may be misleading, in particular for the broad bands of the hydrogen-bonding region (3000−3600 cm^{-1}).

All spectral fits shown in this paper were performed using the software package *IGOR* (version 4.0.5.1). For the Raman and ATR spectra, built-in algorithms were used to fit the spectra to Gaussian and Voigt line shapes, respectively. In the case of the SFG spectra, a Lorentzian fitting function written to incorporate phase was invoked by *IGOR* to fit the spectra.

As shown in the Results and Discussion section, error bars are plotted for the deconvoluted peak areas for the Raman and ATR spectra, as well as SFG spectra. The error bars were obtained as follows. For the Raman and ATR data, the error bars for the peak areas were computed by the fitting algorithm used by *IGOR* and appear in the output. In the case of the SFG data, the error bars were calculated by an entirely different method. Two sets of spectra were obtained of neat water and the salts over a period of several days. The error bars are the standard deviations obtained from the two independent fits.

Line Shapes. All Raman spectra were fit to pure Gaussians, ATR-FTIR spectra were fit to a Voigt line shape, and all SFG spectra were fit to pure Lorentzians. The spectral line shapes depend on line-broadening mechanisms as well as instrumental factors. Homogeneous line-broadening leads to a Lorentzian line shape, while inhomogeneous line-broadening leads to a Gaussian line shape. In general, both line-broadening mechanisms occur in liquids. The differences in line shapes for the three different spectra are most likely due to instrumental factors.[20]

Surface Tension. Surface tensions were measured using a surface tensiometer using the Wilhelmy method (DeltaPi, Kibron Inc., Finland). Values are averages of four measurements conducted at 23 °C.

Chemicals. All the salts studied are available commercially. The salt solutions were made using Nanopure water (resistivity 18−18.2 MΩ cm) and filtered using a carbon filter (Whatman Carbon-Cap) to remove organic impurities. (IR and Raman spectra of the filtered solutions revealed no organic contamination. Moreover, SFG spectroscopy is much more sensitive to organic contamination, and the solutions used for all measurements described in this paper were free of organic contamination as revealed by the SFG spectra.) The concentration of the salts was monitored via the sulfate and/or the ammonium bands using ATR-FTIR.

Computational Method. The salt solution bulk region between two interfacial layers was modeled using MD simulation in a slab arrangement.[21] The slab geometry was realized by employing three-dimensional periodic boundary conditions with an elementary box extended in one dimension. Simulations were performed for three different 1.2 M aqueous salt solutions. In each case, the unit box measuring $3 \times 3 \times 10$ nm^3 contained 864 water molecules and either 36 NH_4^+ and 18 SO_4^{2-}, or 36 Na^+ and 18 SO_4^{2-}, or 18 NH_4^+ and 18 Cl^-. For the ammonium sulfate solution, we also performed simulations with the system size doubled, resulting in a thick slab with 1728 H_2O, 72 NH_4^+, and 36 SO_4^{2-} placed in a $3 \times 3 \times 19.2$ nm^3 unit box.

In all MD simulations, a polarizable force field was employed. Namely, for water, we used the POL3 potential,[22] the sodium and chloride parameters were the same as in our previous studies,[23] and for ammonium, a nonpolarizable potential[24] was employed adding a polarizability of 1.34 Å^3 on the nitrogen atom. For sulfate, we developed a polarizable potential recently.[25] Because of the large polarizability of SO_4^{2-}, simulations of its aqueous solutions suffer from the so-called polarization catastrophe.[26] To circumvent this problem, we therefore reduced the polarizability of each sulfate oxygen to 1.4 Å^3 (i.e., by 20%) (as done in our previous study[27]), rather than increasing the size of the dianion.[25] Calculations were performed using the MD code *Amber 6*.[28]

Results and Discussion

Surface Tension Measurements. The surface tension of aqueous salt solutions of 1 M $(NH_4)_2SO_4$, 1 M Na_2SO_4, 1 M NH_4Cl, 2 M NH_4Cl (to compare the results for the same number of ammonium ions in $(NH_4)_2SO_4$ and NH_4Cl), and neat water were measured at 23 °C and are plotted in Figure 1. The values are given in Table 1 and are consistent with previously reported values.[29] The results show the expected increase in surface tension with an increasing number of ions or ionic multiplicity (compare the surface tensions of $(NH_4)_2SO_4$ and Na_2SO_4 with that of 1 M NH_4Cl), as well as with increasing solute concentration (as shown for 1 M and 2 M NH_4Cl). The surface tension of 1 M NaCl is also plotted (open square) to illustrate that NH_4Cl and NaCl (which contain the same number of ions of the same multiplicity) show a similar increase in surface tension. The relatively large increase in surface tension of the sulfate solutions with respect to neat water and solutions of monovalent halides implies, via the Gibbs adsorption equation,[30] that their aqueous interfaces are practically devoid of ions.

Molecular Dynamics Simulations. The integrated depletion of ions from the surface layer deduced from surface tension measurements is also borne out from MD simulations, which provide a detailed picture of the full interfacial region with

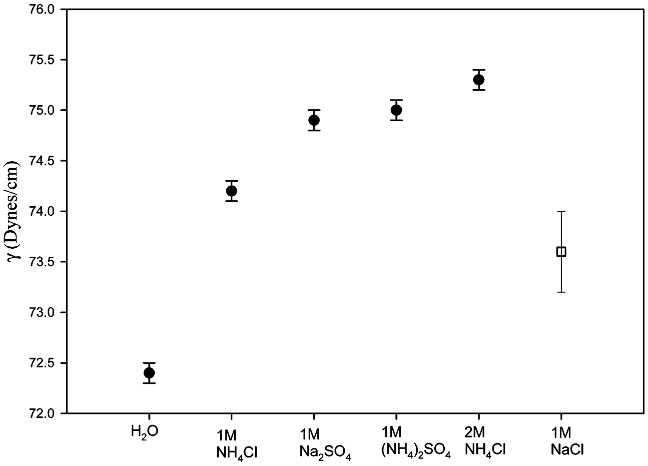

Figure 1. Plot of the surface tension of the aqueous salt solutions at 23 °C.

TABLE 1: Surface Tension of Aqueous Salt Solutions at 23 °C[a]

solution	surface tension γ (mN/m)
H_2O	72.4 (0.1)
1 M NH_4Cl	74.2 (0.1)
1 M Na_2SO_4	74.9 (0.1)
1 M $(NH_4)_2SO_4$	75.0 (0.1)
2 M NH_4Cl	75.3 (0.1)
1 M NaCl	73.6 (0.4)

[a] The measured values are consistent with previously reported values.[29]

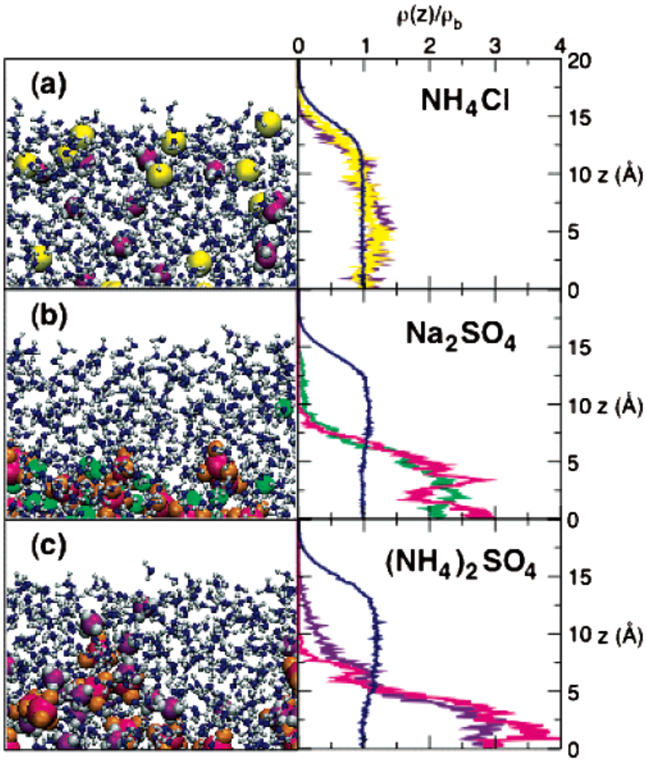

Figure 2. Left panels: snapshot from MD simulations of 1.2 M aqueous solutions of (a) ammonium chloride, (b) sodium sulfate, (c) ammonium sulfate. Right panels: corresponding density profiles of salt ions and water oxygens from the center of the slab ($z = 0$) to the air/water interface. Coloring scheme: H, gray; water O, blue; chloride, yellow; sodium, green; ammonium N, purple; sulfate S, pink; sulfate O, orange.

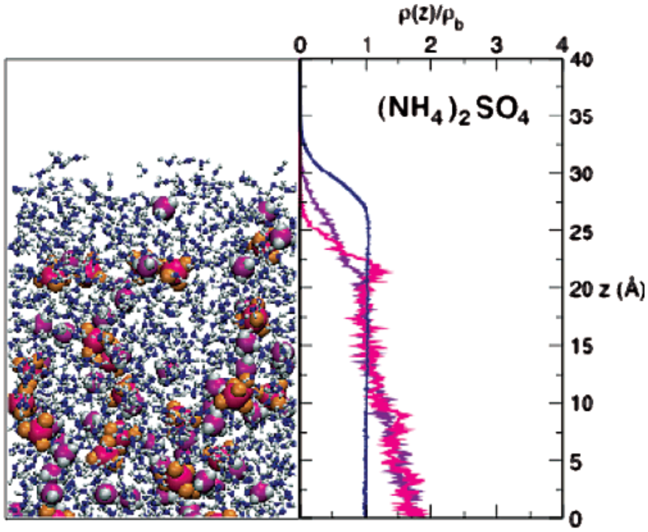

Figure 3. Left panel: snapshot from an MD simulation of a 1.2 M aqueous solution of sodium sulfate for a slab with doubled thickness and, consequently, doubled number of atoms as compared to Figure 2c. Right panel: corresponding density profiles. The coloring scheme is the same as in Figure 1.

molecular resolution. Figure 2 shows the density profile of water oxygens and of the individual ionic species across the slab for 1.2 M solutions of NH_4Cl, Na_2SO_4, and $(NH_4)_2SO_4$, along with snapshots from the simulations of each system. All these profiles were obtained by averaging the ion distributions over a nanosecond MD trajectory. All plotted values are averages over the two halves of the slab. The interface is defined by the concentration gradient of the different species and by the lack of an inversion center (and is hence SFG active), while the bulk is defined as the region where the concentrations are homogeneously mixed and has a macroscopic center of inversion.

Aqueous ammonium chloride (see Figure 2a) behaves qualitatively similarly to sodium chloride, which was investigated earlier.[31] Namely, the cations are repelled from the surface, and chloride anions reside closer to the surface than ammonium ions. Quantitatively, NH_4^+ moves about 1 Å closer to the surface than Na^+, and consequently, the difference between the cationic and anionic density profiles in the interfacial region is smaller in aqueous NH_4Cl than in aqueous NaCl.

Figure 2b, which depicts the ionic density profiles for aqueous sodium sulfate, demonstrates the dramatically different surface behavior of multiply charged ions. The electrostatic penalty of bringing the sulfate dianion close to the surface is large; therefore, SO_4^{2-} solvates deeper in the interfacial region, leaving a roughly 7 Å thick anion-free surface layer. The sodium cations are inherently less “surface-phobic”; however, at 1.2 M, the ion−ion interactions are strong enough to move them also deeper into the interface. Nevertheless, the signal from sodium cations disappears slightly closer to the surface than that of the sulfate dianions.

The ionic density profiles of aqueous $(NH_4)_2SO_4$ are similar to those of Na_2SO_4, with strong repulsion of all the ions from the surface region. This indicates that it is primarily the sulfate dianion which dictates the ionic distribution (compare parts b and c of Figure 2). Nevertheless, we observe certain cationic specificity; namely, ammonium ions penetrate slightly closer to the surface than sodium ions, a behavior that we already observed when chloride was the counteranion. Also, note that in both sulfate solutions the strong ion repulsion from the air/water interface results in an increased concentration of ions in the center of the slab, well above the nominal 1.2 M value. At

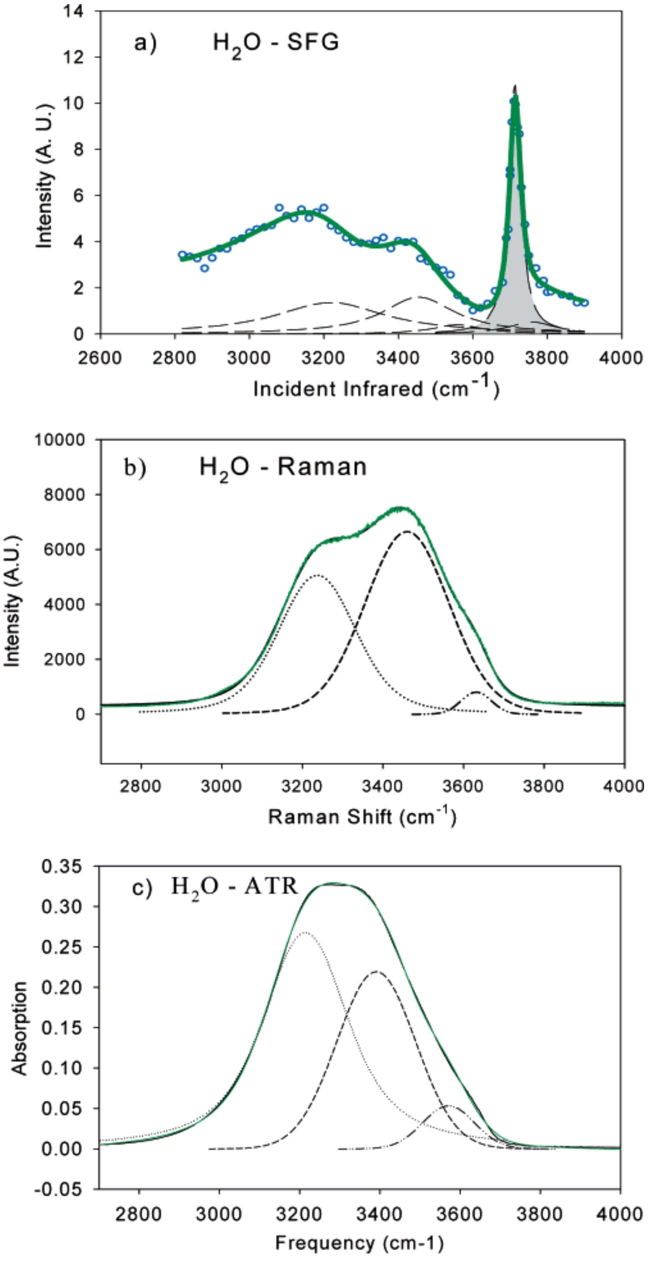

Figure 4. (a) SFG SSP-polarized spectrum of neat water in the O−H stretching region (the deconvoluted peaks shaded in gray have "−" phase, while those which are not shaded have "+" phase). (b) Isotropic Raman spectrum of neat water. (c) ATR-IR spectrum of neat water. The calculated spectra from the spectral fits are shown in green.

these relatively high concentrations and because of the presence of multiply charged ions, a certain degree of ion clustering is observed.

While for solutions of monovalent ions, our slab is thick enough for the ionic density profiles to reach roughly constant values in the central region of the slab (see Figure 2a), this is not completely true for the aqueous sulfate. We have, therefore, performed an additional simulation of 1.2 M ammonium sulfate in a slab with a doubled thickness, to test the convergence of the ionic surface behavior with system size. The results of this large simulation, depicted in Figure 3, show that indeed the interfacial ionic profiles were already semiquantitatively converged in the smaller slabs. In particular, the width of the ion-free surface layer is about the same in the smaller and larger systems, despite the fact that the effective ion concentrations in the bulk regions are different. Apparently, even for the smaller system, the bulk concentration is not high enough to cause precipitation or creation of a different phase, although some degree of ion clustering is clearly observed. The same situation is also anticipated for aqueous sodium sulfate, where the sulfate density profile is almost the same as for ammonium sulfate. Also, note that even in the larger aqueous ammonium sulfate system the ionic densities do not quite level off in the center of the slab. This demonstrates that the interfacial region with varying ionic densities is significantly thicker in aqueous solutions of multiply charged ions compared to those of monovalent ions.

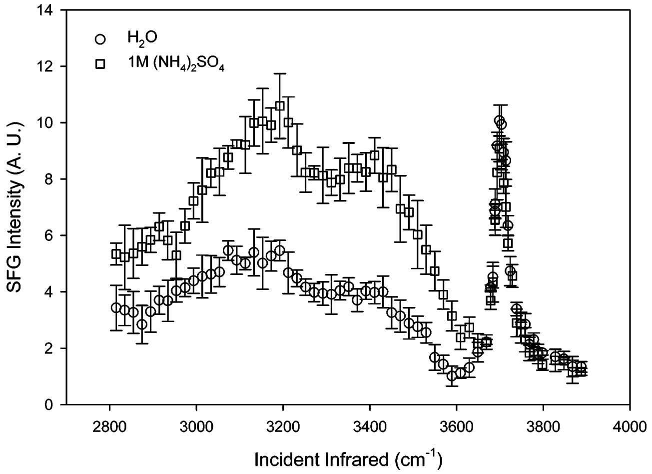

Figure 5. SFG SSP-polarized spectrum of 1 M aqueous ammonium sulfate compared to that of neat water.

Spectroscopy − Spectral Assignments. SFG spectra were taken of 1 M $(NH_4)_2SO_4$, 1 M Na_2SO_4, and 2 M NH_4Cl to directly study the air−liquid interface and to test the MD simulations. The SFG (SSP polarizations in the OH stretch region (∼2900−3900 cm^{-1}) of the air−neat-water interface), isotropic Raman, and ATR-FTIR spectra of neat water are shown in Figure 4a−c, respectively, along with their calculated fits including the component peaks. There are several published SFG spectra of the neat air−water interface.[32−36] The spectral features observed in our neat water surface SFG spectra are similar to previously published neat water SFG spectra.[32−36]

The broad peaks in the 3000−3600 cm^{-1} region contain two prominent bands in the SFG, Raman, and IR spectra of neat water and are positioned at ∼3250 and ∼3450 cm^{-1}. Generally following spectral assignments for ice,[37] and considering the increase in disorder of a noncrystalline system, the 3250 cm^{-1} peak in the Raman (3253 cm^{-1}) and IR (3215 cm^{-1}) spectra is attributed to the vibrational modes from four oscillating dipoles of four-coordinate hydrogen-bonded water molecules. These collective vibrations can be viewed as possessing symmetric character. In the SFG spectrum (peak at ∼3200 cm^{-1}) of neat water, this peak is attributed predominantly to the three-coordinate water molecules at the surface that are single-proton-donor−double-proton-acceptor (DAA),[38−41] with minimal, if any, contribution from four-coordinate interfacial oscillating dipole modes. We assign the 3450 cm^{-1} peak in the Raman, IR, and SFG spectra to the more asymmetrically oscillating dipoles from four-coordinate hydrogen-bonded water molecules. This spectral region can also be described as arising from four-coordinate water molecules where one hydrogen is a poor hydrogen bond donor. The 3450 cm^{-1} peak intensity is significant in the SFG spectrum as revealed through deconvolution of the spectrum into the component peaks, as shown in Figure 4a, which is consistent with recent water cluster IR studies.[38,40] The peak at ∼3550 cm^{-1} in the SFG (∼3550 cm^{-1}),

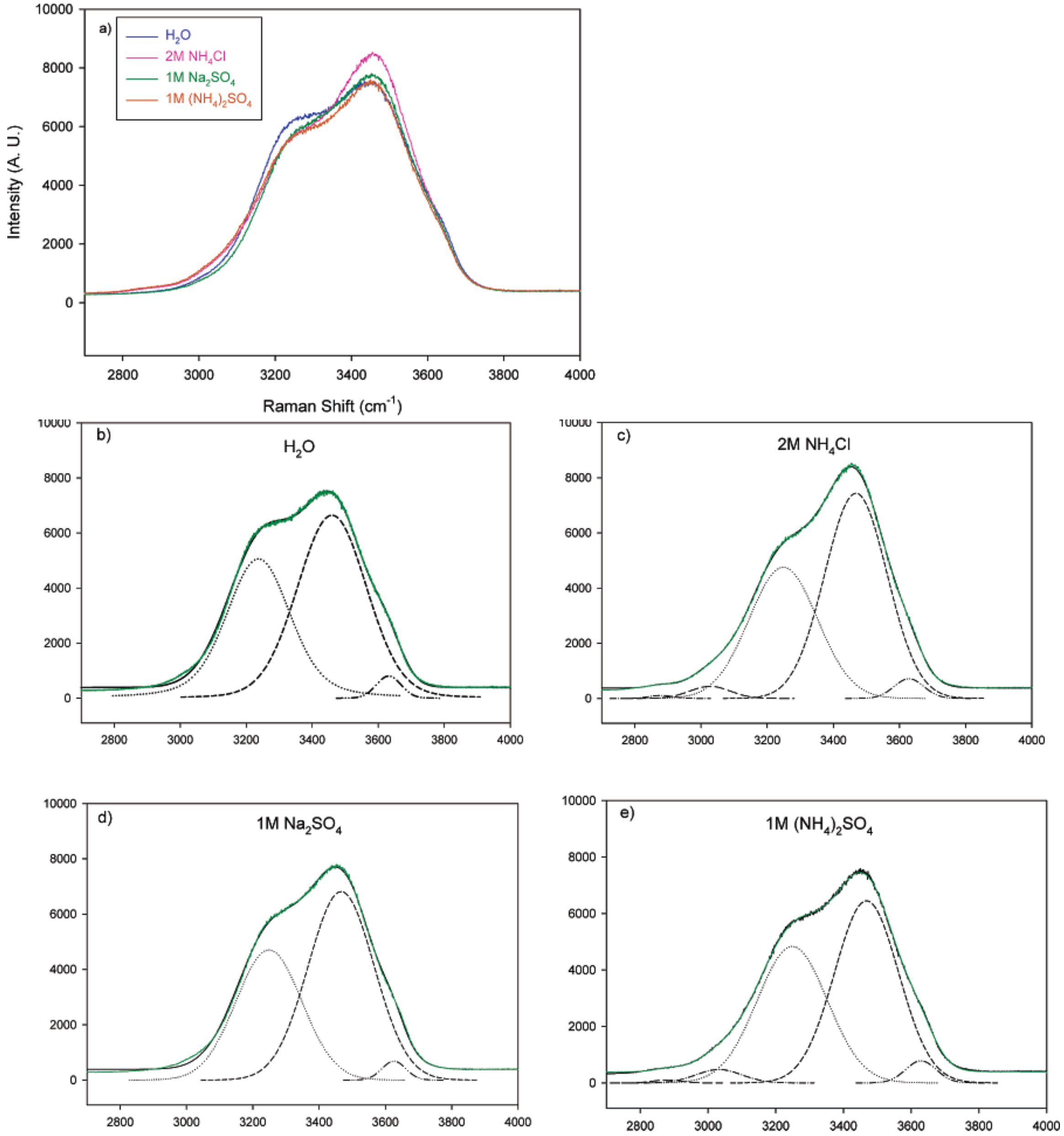

Figure 6. (a) Isotropic Raman spectra of various salt solutions compared to that of neat water; (b−e) spectral fits of Raman spectra. The fitted spectral profile is shown in green.

Raman (3630 cm^{-1}), and IR (3571 cm^{-1}) spectra[42,43] is assigned to the modes associated with three-coordinate asymmetrically hydrogen-bonded water molecules in which one O−H bond is involved in strong hydrogen bonding and the other is only weakly hydrogen-bonded.[42] For the SFG, these three-coordinate species are double-proton-donor−single-proton-acceptor (DDA) molecules.[38−41] The narrow peak at 3700 cm^{-1} in the SFG spectrum of Figure 4a is assigned to the dangling OH (surface free OH) stretch of water molecules that straddle the interface with one non-hydrogen-bonded OH directed into the air phase[32,34,35] and the other OH interacting through hydrogen bonding with the liquid phase as described already within the ∼3250 cm^{-1} SFG peak assignment.[39−41] The assignment of the component peak at ∼3750 cm^{-1} in the SFG spectrum of neat water is still under debate; however, recent discussions[44] point to frustrated rotations of surface water molecules that are hydrogen-bonded via the oxygen (single- and double-acceptor only water molecules). In summary, for the SFG, Raman, and IR spectral assignments of neat water, as the frequency increases, the hydrogen-bonding strength decreases and the asymmetric character of the modes increases.

SFG spectra were acquired from the air−aqueous-ammonium-sulfate interface as shown in Figure 5. Comparison of the SFG spectra of neat water and aq $(NH_4)_2SO_4$ clearly show different spectral intensities. There is a significant increase in intensity within the hydrogen-bonding region (2800−3600 cm^{-1}) of the aq $(NH_4)_2SO_4$ relative to that of neat water. To interpret the SFG spectrum of aq $(NH_4)_2SO_4$, a study of aqueous solutions of NH_4Cl and Na_2SO_4 was conducted to determine how individual ions affect the hydrogen-bonding network of water. Raman, IR, and SFG spectra of all salt solutions were obtained to elucidate spectral assignments and interpretation.

The isotropic Raman spectra of the salt solutions in the water O−H stretch region are shown in Figure 6a. Spectral assignments were made after deconvoluting the spectra into component peaks as shown in Figure 6b−e. In the case of aq Na_2SO_4 (Figure 6d), the spectral region between 2800 and 3800 cm^{-1} is essentially from water, because there are no bands from SO_4^{2-}

TABLE 2: Previously Observed NH_4^+ and SO_4^{2-} Raman and IR Bands in $(NH_4)_2SO_4 \cdot 11H_2O$[a]

Raman		IR	
peak position (cm^{-1})	assignment	peak position (cm^{-1})	assignment
980	sulfate symmetric stretch	1103	sulfate asymmetric stretch
2875	second overtone of NH_4^+ umbrella bending	1450	NH_4^+ umbrella bending
3060	combination band of NH_4^+ umbrella bending and rocking	2890	second overtone of NH_4^+ umbrella bending
3115	NH_4^+ symmetric stretch	3060	combination band of NH_4^+ umbrella bending and rocking
3215	NH_4^+ asymmetric stretch	3230−3480 very broad, very intense absorption	

[a] Adapted from ref 45.

TABLE 3: Raman Fit Parameters (Gaussian)

	peak position (cm^{-1})	amplitude	fwhm	area
H_2O	3248.9	6620	243.2	1390540
	3468.4	8724	222.7	1526300
	3628.8	1509	105.9	122730
2 M NH_4Cl	2878.7	110	89.1	10256
	3026.9	440	143.7	67291
	3248.9	4757	243.3	1232330
	3468.4	7440	222.5	1762110
	3628.8	714	106.2	80842
1 M Na_2SO_4	3248.9	4708	233.0	1167870
	3468.4	6813	234.2	1698320
	3628.8	683	84.0	61067
1 M $(NH_4)_2SO_4$	2878.7	107	92.6	10574
	3032.1	472	159.2	79990
	3248.9	4837	243.3	1252760
	3468.4	6451	222.5	1527830
	3628.8	781	106.2	88312

or HSO_4^- in this region. The spectra are assigned as discussed already in the neat water assignments. In the case of aq $(NH_4)_2SO_4$ (Figure 6e) and NH_4Cl (Figure 6c) however, the isotropic Raman spectra show that this spectral region can be complicated by NH_4^+ bands.[45] Spectra of 2 M NH_4Cl were obtained in order to compare the effect of the same number of NH_4^+ ions on the structure of water in aq $(NH_4)_2SO_4$ and NH_4Cl. The peak positions and assignments of vibrational bands previously observed in Raman and IR spectra of aqueous ammonium sulfate of composition $(NH_4)_2SO_4 \cdot 11H_2O$[45] are given in Table 2. These were used as a guide to fit the spectra of the salt solutions. In the case of the ammonium salts, two additional peaks (other than the water peaks) assigned to the second overtone of the NH_4^+ umbrella bend (at ~2880 cm^{-1}) and a combination band of the NH_4^+ umbrella bending and rocking vibrations (at ~3035 cm^{-1}) are observed in our Raman spectra and are in agreement with the Raman study of Spinner.[45] The peak positions, amplitudes, full width at half-maximum (fwhm), and peak areas for the Raman spectra are collected in Table 3.

Deconvolution of the NH_4^+ bands in the 3000−3500 cm^{-1} region is nontrivial. In addition to the two bending modes, there are two fundamental vibrational modes involving the NH_4^+ stretch observed by Spinner: a symmetric stretch in aqueous ammonium sulfate of composition $(NH_4)_2SO_4 \cdot 11H_2O$ at 3115 cm^{-1} and an asymmetric stretch assigned at 3215 cm^{-1}.[45] In the Raman studies conducted on a solution of even this high a concentration, the spectral depolarization ratios of both peaks could not be measured because of the overlap with the water O−H stretch as well as the 3060 cm^{-1} NH_4^+ combination band (see Table 2). In the case of a 1 M solution of $(NH_4)_2SO_4$, the 3100−3200 cm^{-1} region is overwhelmed by the water O−H stretch, and thus, these peaks could not be fit.

The ATR-IR spectra of the salt solutions in the water O−H stretch region are shown in Figure 7a. As in the case of the Raman spectra, the IR spectrum of aq Na_2SO_4 (Figure 7d) in this region can be assigned to the vibrational modes from the hydrogen-bonding network from water. Again, these assignments were made after deconvoluting the spectrum into component peaks as shown in Figure 7d. In the case of the aq ammonium salts, three additional peaks (other than the water peaks) were fit to the spectra as shown in Figure 7c,e for aq NH_4Cl and $(NH_4)_2SO_4$, respectively. These peaks at ~2880, ~3060, and ~3200 cm^{-1} were assigned (using previously observed IR band frequencies shown in Table 2 as a guide) to the second overtone of the NH_4^+ umbrella bend, the combination band of the NH_4^+ umbrella bending and rocking vibrations, and the asymmetric NH_4^+ stretch, respectively. The peak positions, amplitudes, fwhm, and peak areas for the ATR-IR spectra are collected in Table 4.

The SFG (SSP polarized) spectra of the salt solutions are shown in Figure 8a. The average of four SFG spectra for each species is plotted. All the peaks in the spectral region 2800−3900 cm^{-1} for the aqueous salt solutions are assigned to the air−water interfacial O−H stretching modes as discussed already for the SFG spectrum of neat water. However, the 3250 cm^{-1} peak intensity increases for the sodium and ammonium sulfate solutions are attributed to vibrational modes of the four oscillating dipoles of interfacial four-coordinate water oxygens. In the case of Na_2SO_4 (Figure 8d), the assignments are quite unambiguous; however, in the case of the ammonium salts, the NH_4^+ bands observed in the Raman (at ~2880 and ~3040 cm^{-1}) and ATR-IR spectra (at ~2880, ~3060, and ~3200 cm^{-1}) introduce a complication, because they overlap with the O−H stretching region of water. The 2880 and 3060 cm^{-1} peaks are weak in both the Raman and ATR-IR spectra and thus are expected to be weak in the SFG spectra as well (because the SFG intensity is proportional to the product of the Raman and IR transition moments, as per eq 7). The NH_4^+ stretch vibrations could not be assigned in the Raman spectra as mentioned before; thus, their assignment in the SFG spectra would be highly ambiguous and was not incorporated in the spectral fits (although given the broadness and lower signal-to-noise ratio of the SFG spectra compared to Raman and IR spectra, additional peaks can be force-fitted). The spectral fits of the SFG spectra after deconvolution into component peaks are shown in Figure 8b−e with the corresponding spectral parameters given in Table 5.

Spectroscopy and Molecular Dynamics Simulations − Discussion. The intensity of the ~3250 cm^{-1} peak from the

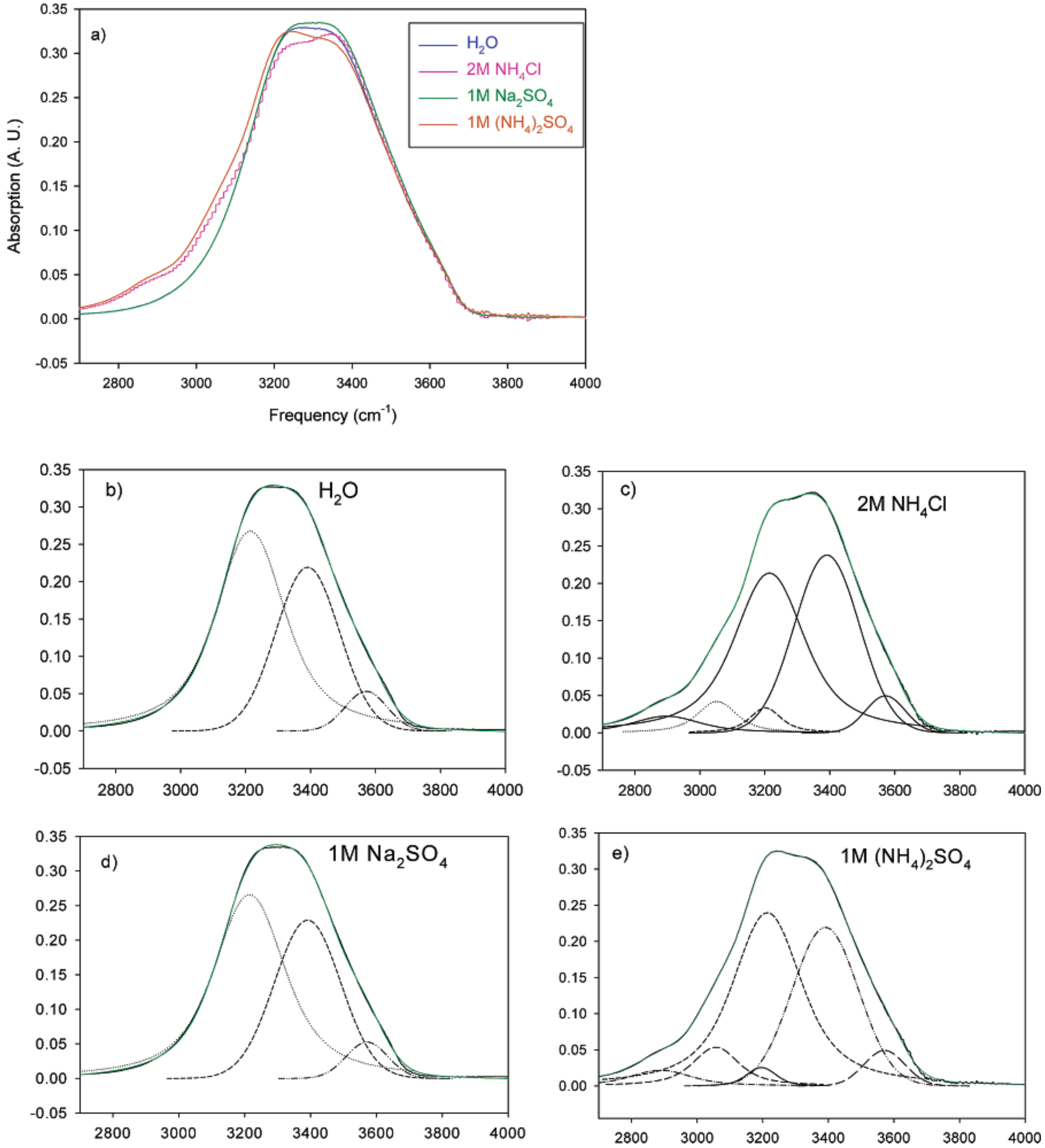

Figure 7. (a) FTIR-ATR spectra of various salt solutions compared to that of neat water; (b−e) spectral fits of ATR spectra. The fitted spectral profile is shown in green.

salt solutions relative to that of neat water from the SFG spectra is shown in Figure 9a. The corresponding isotropic Raman × IR intensities are plotted for comparison with the SSP polarized SFG intensities (recall that the SFG intensity is proportional to the square of the product of the Raman and IR transition moments as well as the square of the number density (*N*), as per eq 7). The Raman × IR intensities show that the intensity of the 3250 cm^{-1} peak decreases to a small extent for all the salt solutions as compared to water, generally driven by the cation and anion replacing water molecules in the sampling volume consistent with the Raman results in Figure 6a. However, in the SFG spectra, the intensity of the ∼3250 cm^{-1} peak increases in the order: $H_2O \approx 2$ M $NH_4Cl < 1$ M $Na_2SO_4 < 1$ M $(NH_4)_2SO_4$. An increase in the Raman and IR transition moment in the salts as compared to water can be ruled out, because the product of the Raman and IR intensities actually decreases in the 3250 cm^{-1} peak (the product of the Raman and IR intensity is proportional to the product of the square of the respective transition moments). In addition to an increase in intensity in the 3250 cm^{-1} peak, there is also an increase in intensity in the 3450 cm^{-1} peak in aq Na_2SO_4 and $(NH_4)_2SO_4$, which is shown in Figure 9b. Similar to the analysis of the 3250 cm^{-1} band, an increase in the Raman × IR transition moments of the 3450 cm^{-1} band in the salt solutions as compared to neat water is ruled out as the full cause, because the SFG intensity enhancement in Na_2SO_4 and $(NH_4)_2SO_4$ spectra is much larger than the Raman × IR enhancement.

Another explanation for the enhancement of the 3250 and 3450 cm^{-1} bands in the SFG spectra of Figure 8d,e could be an increased ordering of the interfacial water molecules under the influence of a local weak electric field induced by the sulfate dianions in aq Na_2SO_4 and $(NH_4)_2SO_4$ and/or an increase in the interfacial depth. (Recall that the SFG intensity is proportional to the square of the number density (*N*), as per eq 7, and that the intensities from the SSP polarized SFG spectra increase if the water molecules are better aligned with their transition

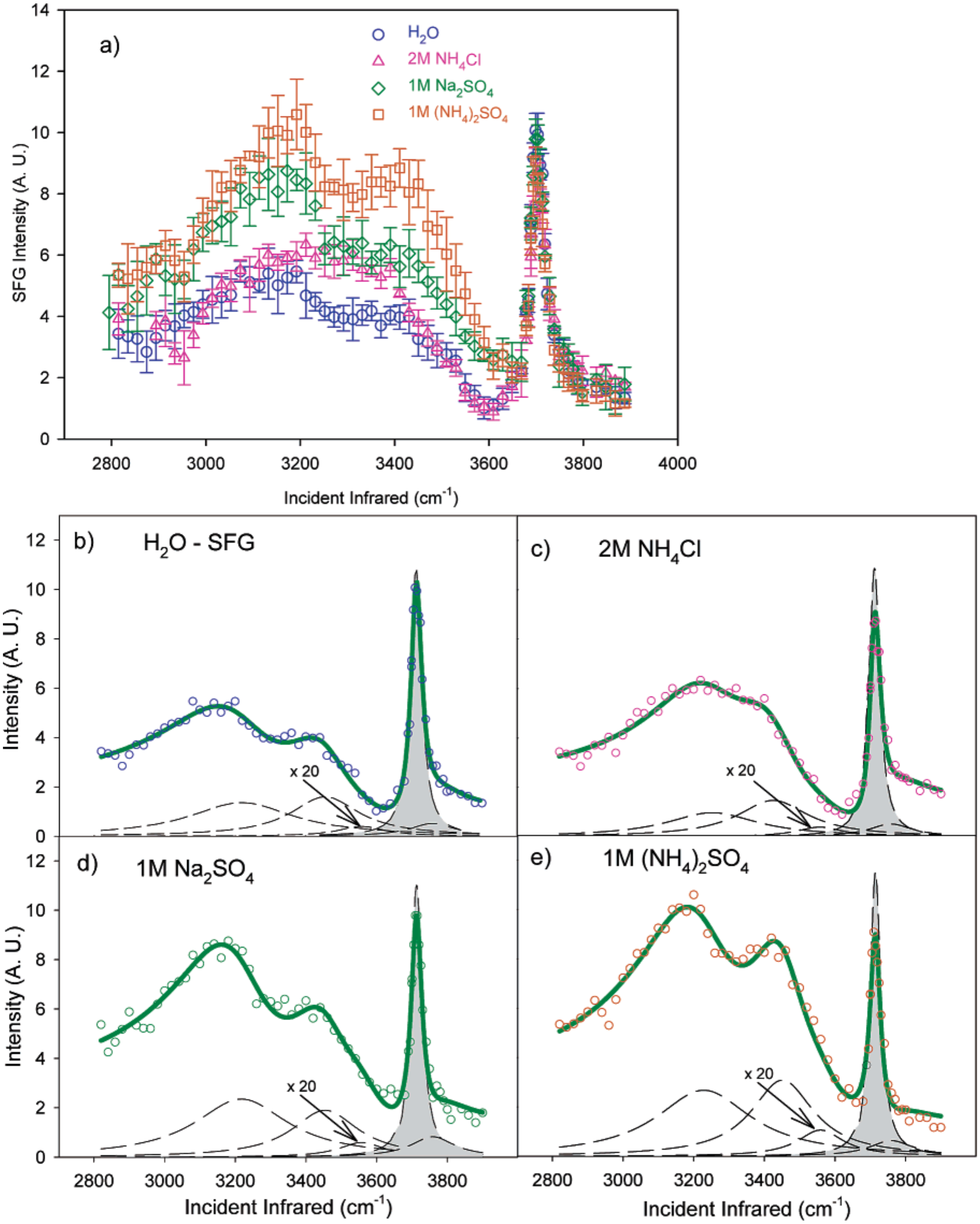

Figure 8. (a) SFG SSP-polarized spectra of various salt solutions compared to that of neat water; (b−e) spectral fits of SFG spectra. The green solid line shows the fitted spectral profile. The component peaks shaded in gray have "−" phase, while those which are not shaded have "+" phase.

moments normal to the surface, yet cancellation will occur if the vectors oppose each other.) The local weak electric field effect excludes the solvation shell water molecules that partially contribute to the 3450 cm^{-1} band of the salt solutions, although these molecules will minimally contribute with increasing interfacial depth. The explanation presented here is consistent with the MD simulations on the aqueous solutions of NH_4Cl, Na_2SO_4, and $(NH_4)_2SO_4$ shown in Figure 2a−c and Figure 3, as discussed above.

To further explore the localized field effect, we turn to the MD simulations. Because the SFG contribution from molecules in centrosymmetric environments vanishes, the inhomogeneous interfacial region probed by the SFG experiments is better defined in terms of the region over which there is a net orientational polarization of water molecules. To this end, in Figure 10, we have plotted $\langle \cos \theta \rangle$, as a function of location in slabs of neat water and two ammonium salts, 1.2 M NH_4Cl (i.e., salt with a monovalent anion), and 1.2 M $(NH_4)_2SO_4$ (i.e., a representative of a salt with a divalent anion). Here, θ is the angle between a water dipole moment and a vector normal to the slab surface (i.e., the z axis in the simulation cell), and the angular brackets denote an average over time and molecules. This quantity vanishes for an isotropic distribution of water orientations and is nonzero where there is a net orientation of

TABLE 4: FTIR-ATR Fit Parameters (Voigt)

	peak position (cm^{-1})	amplitude	fwhm	area	Voigt shape
H_2O	3214.6	0.30	251.0	95	1.00
	3391.1	0.20	231.3	54	0.00
	3571.3	0.05	152.0	9	0.00
2 M NH_4Cl	2897.1	0.03	245.4	8	1.03
	3052.6	0.05	141.6	8	1.00
	3201.6	0.04	114.0	5	1.10
	3214.6	0.30	252.5	76	1.00
	3391.1	0.20	235.8	60	0.00
	3571.3	0.05	142.4	8	0.00
1 M Na_2SO_4	3214.6	0.30	254.0	95	1.00
	3391.1	0.23	236.7	58	0.00
	3571.3	0.05	148.9	8	0.00
1 M $(NH_4)_2SO_4$	2888.4	0.02	217.9	6	0.79
	3056.9	0.06	163.8	12	1.00
	3195.7	0.03	105.3	3	0.40
	3214.6	0.30	246.5	83	1.00
	3391.1	0.20	238.1	56	0.00
	3571.3	0.05	146.8	8	0.00

TABLE 5: SFG Fit Parameters (Lorentzian)

	peak position (cm^{-1})	phase	amplitude	fwhm	area
H_2O	3207.9	+	210.1	180.3	601.6
	3444.6	+	137.4	117.6	433.0
	3547.0	+	21.9	78.0	17.3
	3703.1	−	62.4	19.1	627.6
	3748.5	−	58.8	74.9	119.2
2 M NH_4Cl	3242.8	+	155.9	158.0	392.5
	3414.9	+	159.0	122.5	555.1
	3547.5	+	21.3	78.7	16.2
	3701.8	−	60.1	19.2	613.5
	3748.5	−	55.2	74.8	106.7
1 M Na_2SO_4	3207.3	+	246.9	160.9	956.3
	3444.1	+	158.9	114.1	600.3
	3547.9	+	22.7	78.4	18.5
	3703.2	−	62.4	17.5	686.7
	3748.5	−	58.1	74.9	116.3
1 M $(NH_4)_2SO_4$	3218.4	+	267.5	163.5	1103.9
	3441.4	+	188.7	107.4	907.6
	3549.3	+	25.6	78.4	23.4
	3704.9	−	62.4	18.4	653.8
	3749.5	−	59.2	74.2	121.7

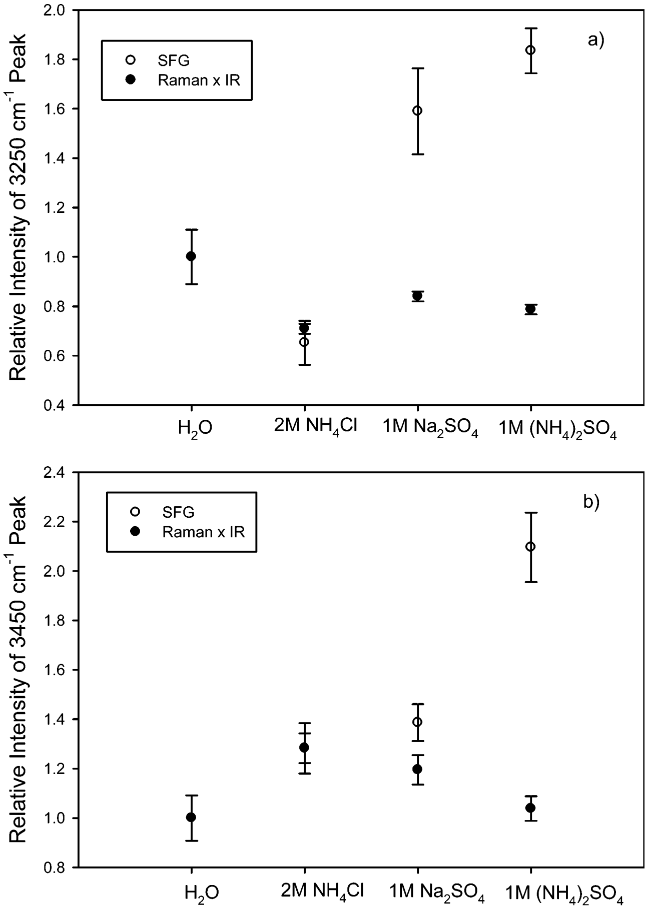

Figure 9. (a) Plot of the relative (to water) intensities of the 3250 cm^{-1} peak. (b) Plot of the relative (to water) intensities of the 3450 cm^{-1} peak. The relative intensities from the SFG spectra are compared with the product of the relative intensities of the corresponding peaks from the isotropic Raman and IR spectra.

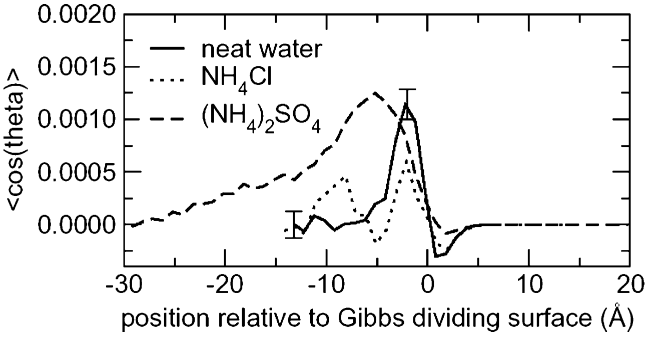

Figure 10. Orientation polarizations (see text for details) from MD simulations as functions of position in the slabs relative to the Gibbs dividing surface (defined as the position where the water density is equal to one-half its bulk value). Representative statistical uncertainties, taken as the standard deviations of averages computed over 200 ps blocks, are indicated by the error bars.

water dipoles. The orientational polarization and other quantities reported in Figure 10 for $(NH_4)_2SO_4$(aq) were obtained from the simulation of the thicker system only because data obtained for the smaller system appeared to contain finite size artifacts.

The data plotted in Figure 10 show that the interface, defined by nonzero values of ⟨cos *θ*⟩, increases in width in the order H_2O < NH_4Cl(aq) < $(NH_4)_2SO_4$(aq). The maximum degree of water orientational polarization is roughly the same in neat water and $(NH_4)_2SO_4$(aq), and roughly twice that of NH_4Cl(aq). In neat water, the orientational ordering is confined mostly to the surface layer, while in the NH_4Cl solution, there appears to be an ordered subsurface layer about 10 Å below the Gibbs dividing surface in addition to an ordered surface layer. The orientational polarization decays slowly into the $(NH_4)_2SO_4$ solution, such that the width of the region over which water molecules have an appreciable net orientation is approximately 20 Å. This is consistent with the increase in SFG intensity of the 3000−3600 cm^{-1} region for the $(NH_4)_2SO_4$ (Figure 5 and Figure 8a,e).

The thickening of the interface can contribute to the increase in the SFG intensity in the 3250 and 3450 cm^{-1} regions from the sulfate solutions. It is not possible to distinguish between SFG signal enhancement because of ordering of water molecules under the presence of a weak electrostatic field and an increase in interfacial depth. However, the thickening of the interface is supported by orientation polarizations (Figure 10) and density profiles (Figure 2b,c; Figure 3), which reveal that the interfacial depth increases in aq Na_2SO_4 and $(NH_4)_2SO_4$ (the density gradient extends over a larger region) as compared to aq NH_4Cl (Figure 2a). The interface is defined by the concentration gradient of the different species and lacks an inversion center (and is hence SFG active), while the bulk is defined as the region where the species are homogeneously mixed and therefore has a macroscopic center of inversion (and is hence SFG inactive). Thus, we conclude that the air–aqueous interface of the ammonium sulfate solution (as well as the sodium sulfate solution) has widened and that local field effects caused by the sulfate dianions play a significant role in this interfacial behavior of water. These effects thereby account for the larger 3250 and the 3450 cm^{-1} peak intensities observed in the aq $(NH_4)_2SO_4$ and the Na_2SO_4 SFG spectra (Figures 8 and 9).

To gain further insight into the SFG spectra, in addition to knowing the extent of structural inhomogeneity, it is also relevant to quantify the populations of water OH bonds in various settings. To this end, the water molecules are divided into three general groups: (1) those for which both OH bonds are hydrogen bond donors (2D) to other water molecules, (2) those for which one OH bond is free and one is involved in a hydrogen bond with another water molecule (1D), and (3) those for which both OH bonds are free (i.e., not involved in any hydrogen bonds) (0D). Water molecules involved in ion–water hydrogen bonds were excluded to simplify the analysis, and because they make a relatively insignificant contribution to the SFG spectra at the concentrations considered here. The surface density (number per unit area) of 2D, 1D, and 0D water molecules is shown as a function of position in the slabs in Figure 11a–c, respectively. A geometric criterion was used to define hydrogen bonds: acceptor oxygen to donor hydrogen distance less than 3.5, 3.8, and 3.5 Å for water–water, water–chloride, and water–sulfate oxygen hydrogen bonds, respectively, and the acceptor O···O–H angle less than 30°. In Figure 11a–c, it is evident that the populations of the three OH species show qualitatively similar variations with position relative to the surface in all three solutions, in contrast to the orientational polarization profiles (Figure 10).

The population of 2D water molecules increases rapidly on passing from the surface to the interior of all three systems (Figure 11a), roughly tracking the water oxygen density profiles (Figures 2 and 3). The population is reduced in the salt solutions compared to neat water, reflecting the replacement of water–water hydrogen bonds by ion–water hydrogen bonds.

The population of the 1D water molecules exhibits a peak in the interfacial layer and decays rapidly to a nearly constant value in the interior of the solutions (Figure 11b). The overall number of 1D waters is slightly larger throughout in neat water than in the salt solutions, again because in the salt solutions some water–water hydrogen bonds are replaced by ion–water hydrogen bonds. There are slightly more 1D waters in the surface layer of $(NH_4)_2SO_4$(aq) compared to NH_4Cl(aq), while in the interior of the solutions, there are slightly more 1D waters in NH_4Cl(aq).

The populations of 0D water molecules (those with two free OH bonds) are very similar in all three systems throughout the slabs. Note that the number of water molecules with one free OH bond (1D) is about an order of magnitude greater than the number with two free OH bonds (0D). Overall, the total number of free OH bonds is similar in the three systems, and this is consistent with the nearly constant intensity in the free OH region (3700 cm^{-1} peak) of the SFG spectra.

In summary, no significant differences between neat water and the salt solutions are observed for the 2D, 1D, or 0D surface densities. This suggests that the interpretation of the SFG spectral differences rests on differences in water orientational order. Recall that water molecules will only contribute to the SFG signal if they are in a non-centrosymmetric environment. Indeed, the greater intensity in the hydrogen-bonded region of the SFG spectra for $(NH_4)_2SO_4$(aq) versus NH_4Cl(aq) and neat water reflects the longer range of orientational ordering (i.e., thicker interfacial region) as shown in Figure 10.

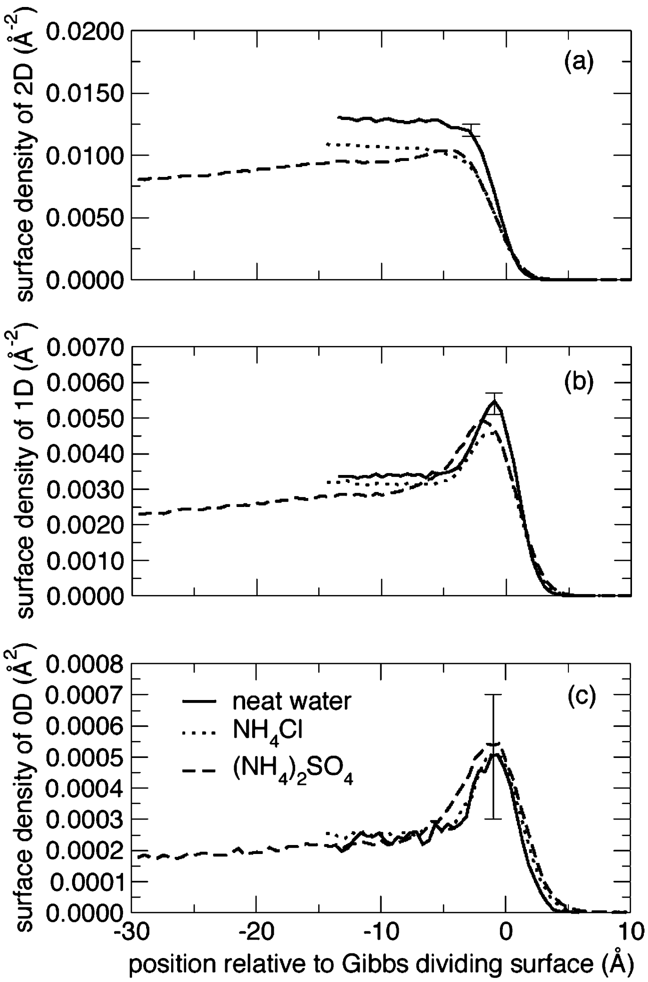

Figure 11. Number of water OH bonds per unit area in water molecules for which: (a) both OH bonds are involved in water–water hydrogen bonds (2D); (b) one OH bond is free and one is involved in a water–water hydrogen bond (1D); both OH bonds are free (0D). The hydrogen bond definition is described in the text. Representative statistical uncertainties, taken as the standard deviations of averages computed over 200 ps blocks, are indicated by the error bars.

Conclusions

The air–liquid interface of aqueous solutions containing ammonium and sulfate ions (NH_4Cl, Na_2SO_4, and $(NH_4)_2SO_4$) was investigated using molecular dynamics simulations and using vibrational sum frequency generation spectroscopy in the O–H stretching region of liquid water. Our SFG results show, after comparison to isotropic Raman and ATR-FTIR spectra, enhanced intensity in the water O–H vibrational modes at the air–liquid interface in aq $(NH_4)_2SO_4$ and Na_2SO_4 compared to aq NH_4Cl and neat water. In the case of aq NH_4Cl, the perturbation of the hydrogen-bonded network of water because of the ions is similar at the interface and the bulk. Furthermore, comparison of interfacial and bulk vibrational structure reveals differences at the air–liquid interface relative to the bulk by ions in aq $(NH_4)_2SO_4$ and Na_2SO_4. The molecular dynamics simulations combined with the SFG results reveal a thickening (widening) of the air–liquid interface for the aq sulfate solutions, which is inclusive of alignment of the interfacial water molecules extending deeper into the bulk solution.

Acknowledgment. Support from the US-NSF (grant CHE-0209719), NSF-CAREER (grant CHE-0134131), and from the Czech ministry of education (grants LC512 and ME644) is gratefully acknowledged. Part of the work in Prague was completed within the framework of research project Z40550506. The authors gratefully acknowledge V. Buch, P. Devlin, and U. Buck for extensive discussions of this work. We also thank D. Liu for assistance.

References and Notes

(1) Anderson, T. L.; Charlson, A. J.; Schwartz, S. E.; Knutti, R.; Boucher, O.; Rodhe, H.; Heintzenberg, J. *Science* **2003**, *300*, 1103.

(2) Crowley, T. J. *Science* **2000**, *289*, 270.

(3) *Climate Change 2001: The Scientific Basis*; Houghton, J. T., Ding, Y., Griggs, D. J., Noguer, M., Linden, P. J. V. d., Dai, X., Maskell, K., Johnson, C. A., Eds.; Cambridge University Press: Cambridge, 2001.

(4) Keene, W. C.; Sander, R.; Pszenny, A. A. P.; Vogt, R.; Crutzen, P. J.; Galloway, J. N. *J. Aerosol Sci.* **1998**, *29*, 339.

(5) Posfai, M.; Anderson, J. R.; Buseck, P. R.; Shattuck, T. W.; Tindale, N. W. *Atmos. Environ.* **1994**, *28*, 1747.

(6) Chelf, J. H.; Martin, S. T. *J. Geophys. Res., [Atmos.]* **2001**, *106*, 1215.

(7) Prenni, A. J.; Wise, M. E.; Brooks, S. D.; Tolbert, M. A. *J. Geophys. Res., [Atmos.]* **2001**, *106*, 3037.

(8) Sander, R.; Lilieveld, J.; Crutzen, P. J. *J. Atmos. Chem.* **1995**, *20*, 89.

(9) Talbot, R. W.; Dibb, J. E.; Loomis, M. B. *Geophys. Res. Lett.* **1998**, *35*, 1367.

(10) Kane, S. M.; Caloz, F.; Leu, M. *J. Phys. Chem. A* **2001**, *105*, 6465.

(11) Donaldson, D. J.; Guest, J. A.; Goh, M. C. *J. Phys. Chem.* **1995**, *99*, 9313.

(12) Finlayson-Pitts, B. J.; Pitts, J. N. *Chemistry of the Upper and Lower Troposphere*; Academic Press: New York, 2000.

(13) Longfellow, C. A.; Imamura, T.; Ravishankara, A. R.; Hanson, D. R. *J. Phys. Chem. A* **1998**, *102*, 3323.

(14) Shen, Y. R. *The principles of nonlinear optics*, 1st ed.; John Wiley & Sons: New York, 1984.

(15) Bloembergen, N.; Pershan, P. S. *Phys. Rev.* **1962**, *128*, 606.

(16) Miranda, P. B.; Shen, Y. R. *J. Phys. Chem. B* **1999**, *103*, 3292.

(17) Hirose, C.; Akamatsu, N.; Domen, K. *Appl. Spectrosc.* **1992**, *46*, 1051.

(18) Moad, A. J.; Simpson, G. J. *J. Phys. Chem.* **2004**, *108*, 3548.

(19) Liu, D.; Ma, G.; Levering, L. M.; Allen, H. C. *J. Phys. Chem. B* **2004**, *108*, 2252.

(20) Stewart, J. E. *Infrared Spectroscopy − Experimental Methods and Techniques*; Marcel Dekker Inc.: New York, 1970.

(21) Wilson, M. A.; Pohorille *J. Chem. Phys.* **1991**, *95*, 6005.

(22) Caldwell, J.; Kollman, P. A. *J. Phys. Chem.* **1995**, *99*, 6208.

(23) Jungwirth, P.; Tobias, D. J. *J. Phys. Chem. B* **2002**, *106*, 6361.

(24) Boudon, S.; Wipff, G. J. *J. Comput. Chem.* **1991**, *12*, 42.

(25) Jungwirth, P.; Curtis, J. E.; Tobias, D. J. *Chem. Phys. Lett.* **2003**, *367*, 704.

(26) Thole, B. T. *Chem. Phys.* **1981**, *59*, 341.

(27) Jungwirth, P.; Rosenfeld, D.; Buch, V. *Atmos. Res.* In Press.

(28) Case, D. A.; Pearlman, D. A.; Caldwell, J. W.; Cheatham, T. E., III; Ross, W. S.; Simmerling, C. L.; Darden, T. A.; Merz, K. M.; Stanton, R. V.; Cheng, A. L.; Vincent, J. J.; Crowley, M.; Tsui, V.; Radmer, R. J.; Duan, Y.; Pitera, J.; Massova, I.; Seibel, G. L.; Singh, U. C.; Weiner, P. K.; Kollman, P. A. *Amber 6*; University of California: San Francisco, 1999.

(29) Washburn, E. W. *International Critical Tables of Numerical Data, Physics, Chemistry, and Technology*; McGraw-Hill: New York, 1928; Vol. 4.

(30) Gibbs, J. W. *The Collected Works of J. W. Gibbs*; Longmans: New York, 1931; Vol. 1.

(31) Jungwirth, P.; Tobias, D. J. *J. Phys. Chem. B* **2001**, *105*, 10468.

(32) Allen, H. C.; Raymond, E. A.; Richmond, G. L. *J. Phys. Chem.* **2001**, *105*, 1649.

(33) Shultz, M. J.; Baldelli, S.; Schnitzer, C.; Simonelli, D. *J. Phys. Chem. B* **2002**, *106*, 5313.

(34) Du, Q.; Superfine, R.; Freysz, E.; Shen, Y. R. *Phys. Rev. Lett.* **1993**, *70*, 2313.

(35) Schnitzer, C.; Baldelli, S.; Campbell, D. J.; Shultz, M. J. *J. Phys. Chem. A* **1999**, *103*, 6383.

(36) Allen, H. C.; Raymond, E. A.; Richmond, G. L. *Curr. Opin. Colloid Interface Sci.* **2000**, *5*, 74.

(37) Buch, V.; Devlin, J. P. *J. Chem. Phys.* **1999**, *110*, 3437.

(38) Brudermann, J.; Melzer, M.; Buck, U.; Kazimirski, J. K.; Sadlej, J.; Buch, V. *J. Chem. Phys.* **1999**, *110*, 10649.

(39) Buck, U.; Ettischer, I.; Melzer, M.; Buch, V.; Sadlej, J. *Phys. Rev. Lett.* **1998**, *80*, 2578.

(40) Devlin, J. P.; Sadlej, J.; Buch, V. *J. Phy. Chem. A* **2001**, *105*, 974.

(41) Pribble, R. N.; Zwier, T. S. *Science* **1994**, *265*, 75.

(42) Scherer, J. R. The vibrational spectroscopy of water. In *Advances in Infrared and Raman Spectroscopy*; Clark, R. J. H., Hester, R. E., Eds.; Heyden: Philadelphia, 1978; Vol. 5, Chapter 3, p 149.

(43) Scherer, J. R.; Go, M. K.; Kint, S. *J. Phys. Chem.* **1973**, *77*, 2108.

(44) Shultz, M. J. Private communication.

(45) Spinner, E. *Spectrochim. Acta, Part A* **2003**, *59*, 1441.